Phase diagram and orbital Chern insulator in twisted double bilayer graphene

Yi-Xiang Wang [1,2,*] Fuxiang Li [2,†] and Zi-Yue Zhang [1]
[1]*School of Science, Jiangnan University, Wuxi 214122, China*
[2]*School of Physics and Electronics, Hunan University, Changsha 410082, China*

(Received 22 September 2020; revised 18 February 2021; accepted 22 February 2021; published 1 March 2021)

Compared with twisted bilayer graphene, twisted double bilayer graphene (TDBG) provides another important platform to realize the moiré flat bands. In this paper, we first calculate the valley Chern number phase diagram of TDBG in the parameter space spanned by the twist angle and the interlayer electric potential. To include the effects of interactions, we then phenomenologically introduce the spin-splitting and valley-splitting. We find that when the valley splitting is larger than the bandwidth of the first conduction band so that a gap is opened and the spin splitting is relatively weak, the orbital Chern insulator emerges at half-filling, associated with a large orbital magnetization (OM). Further calculations suggest that there is no sign reversal of the OM when the Fermi energy goes from the bottom to the top of the half-filling gap, as the OM remains negative in both AB-AB stacking and AB-BA stacking. The implications of our results for the ongoing experiments are also discussed.

DOI: 10.1103/PhysRevB.103.115201

I. INTRODUCTION

The recent discovery of the correlated insulator states [1], superconductivity [2,3], as well as quantum anomalous Hall (QAH) state [4,5] in twisted bilayer graphene (TBG) have drawn significant attention. In TBG, the spatial variation of interlayer coupling modified the Dirac linear band structure of graphene in such a way that the band dispersion was almost completely suppressed at the so-called magic angle [6]. As the bandwidth w of the flat band was sufficiently narrow, it was possible to achieve the situation $\frac{U}{w} \gg 1$ so that the effective Coulomb interaction U dominated the system. The interaction provided a possible mechanism for the observed correlated insulator states and superconducting states upon charge doping [7–9]. It was further revealed that the low-energy flat bands could have well-defined valley Chern numbers, which can host a number of fascinating many-body phenomena, including the fractional QAH effects [10].

This novel twist-angle degree of freedom and its control could be generalized to other two-dimensional systems, where similar correlated physics may also be exhibited. It was demonstrated that twisted double bilayer graphene (TDBG) [11–15] and ABC-stacked trilayer graphene on hexagonal boron nitride (hBN) supperlattices [16,17] can provide another important moiré system with strong correlation effect. TDBG refers to a pair of bilayer graphene twisted with each other by a small angle θ. There may exist as two different stacking types for TDBG, AB-AB stacking and AB-BA stacking, both of which will be considered in this paper. Unlike TBG, the isolated flat moiré band in TDBG can appear when an out-of-plane electric field is applied on the system [18]. More importantly, as the bilayer graphene becomes gapped under the electric field, the opposite Berry curvatures at the two valleys can be accumulated [19,20], leading to the change of the band Chern number. As both the twist angle and the electric field can be well controlled in the experiment, the study of the driven Chern number phase diagram in TDBG is meaningful and gives the first motivation of the present work.

In TBG, the topological flat moiré bands are closely connected to the large orbital magnetizations (OMs), which may give rise to an orbital Chern insulator (OCI) state once the valley symmetry is broken. In fact, the OCI has been successfully observed at $n = \frac{3}{4}n_s$ filling of TBG when aligned with the hBN substrate around the magic angle [4,5], with $n_s = \frac{4}{S_M}$ being the density corresponding to fully filling one moiré band, the factor of 4 accounting for the spin and valley flavors, and S_M denoting the size of the unit moiré cell. The time-reversal symmetry (TRS) breaking mechanism of OCI in TBG can be attributed to the condensation of the electrons in the momentum space, where the many-body interaction drives the spontaneous valley polarization. Another important system called the spin Chern insulator was observed in Cr-doped $(Bi, Sb)_2Te_3$ thin film [21], where the TRS is broken by the local spin moments that are ordered ferromagnetically due to the exchange interaction. Both the orbital and spin Chern insulators are quite different from the Chern insulator identified in the original Haldane model [22], where the TRS is broken by the local staggered magnetic flux in a unit cell, leading to the Berry curvatures of the same sign around the two valleys.

In this paper, we will study under what conditions the OCI can be realized in TDBG. Although in a unit cell, TDBG has two times the sublattices as TBG, the band counting is the same and each moiré band accommodates four electrons per unit moiré cell when the spin-degeneracy and valley-degeneracy are preserved. If the number of electrons per moiré band is a multiple of four, gaps may appear. However, when the Fermi energy lies in the gap, the Chern number vanishes

*wangyixiang@jiangnan.edu.cn
†fuxiangli@hnu.edu.cn

due to the opposite contributions from the two valleys that are connected by the TRS. Thus, to observe the nontrivial Chern insulator phase in TDBG, the four-fold degeneracy of the moiré band needs to be broken, which may be achieved by the spin-splittings and valley-splittings. Moreover, the magnetic property studied in TBG revealed that the OM may reverse its sign when doping the system from the bottom to the top of the insulating gap, and suggested that this was quite common in the OCI [23]. The external perpendicular magnetic field $\boldsymbol{B}$ favors the state with magnetization $\boldsymbol{M}$ aligned in the same direction, leading to the stronger resistive signal in the transport experiment. Thus the sign reversal of the OM can drive a reversal of the valley polarization when the Fermi energy crosses the gap, enabling the electrical switching of a magnetic state in TBG in when a fixed magnetic field is present [24]. Then a natural question arises that what is the magnetic property in TDBG when the OCI is realized, which will also be explored in this paper.

Our main findings are as follows. (i) By using the Fukui's algorithm, we perform accurate calculations of the Chern numbers of the first valence and first conduction band, (C_{v1}, C_{c1}), and obtain a reliable phase diagram of TDBG as a function of the twist angle and the electric potential, especially for the regions where the neighboring moiré bands are overlapped. We find that the phase diagrams for AB-AB stacking and AB-BA stacking show significant discrepancies. Since the $(C_{v1}, C_{c1}) = (2, -2)$ phase in the AB-BA stacking and the (1,1) phase in the AB-BA stacking share similar broad parameter regions, and in the two phases the bands are relatively flat, our studies are mainly focused on these two phases. (ii) By phenomenologically introducing the interaction-induced valley splitting and spin splitting, the OCI state is found at half-filling $n = \frac{1}{2}n_s$ of the first conduction band and is associated with the large OM. The condition is that the valley splitting should be larger than the bandwidth so as to open a gap at half-filling, and the spin splitting should be relatively weak. (iii) For the OCI in TDBG, our calculations suggest that there is no sign reversal of the OM when the Fermi energy goes from the bottom to the top of the half-filling gap, as the OM remains negative in both AB-AB stacking and AB-BA stacking. Our study could help explore the twist-angle and electric-field modulated topological phases of matter in the flat-band twisted superlattice systems.

II. TWISTED DOUBLE BILAYER GRAPHENE MODEL

Bilayer graphene is composed of a pair of monolayer graphene, where four sublattices are included in a unit cell, labeled as A_1, B_1 in the upper layer and A_2, B_2 in the bottom layer. In bilayer graphene, the most stable configuration is AB or BA stacking, which is also the stacking structure of three-dimensional (3D) bulk graphite [25]. In AB (BA) stacking, the A_1 (B_1) sublattice of the upper layer is located on the top of the B_2 (A_2) sublattice of the lower layer, leading to a small on-site energy Δ for these dimer sublattices. The other two sublattices, B_1 and A_2 (A_1 and B_2), are directly above or below the hexagon center of the other layer. The schematics of TDBG are shown in Fig. 1, with the two stacking types, AB-AB stacking and AB-BA stacking.

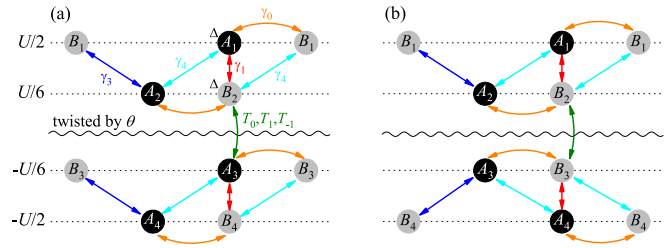

FIG. 1. Schematics of TDBG with (a) AB-AB stacking and (b) AB-BA stacking. The hopping integrals between the neighboring sublattices, $\gamma_{0,1,3,4}$, are shown with arrows in different colors. For the dimer sublattices, there is a small on-site energy Δ. The layer-dependent potentials are also labeled.

To describe the single-particle band structure of TDBG, we adopt the commonly used tight-binding model [6,18,26–29]. In the eight-component basis $(c_{A_1}, c_{B_1}, c_{A_2}, c_{B_2}, c_{A_3}, c_{B_3}, c_{A_4}, c_{B_4})^T$, the Hamiltonian at small twist angle θ is

$$H_{AB-AB}(\boldsymbol{k}) = \begin{pmatrix} h_0(\boldsymbol{k}_1) & g^\dagger(\boldsymbol{k}_1) & & \\ g(\boldsymbol{k}_1) & h_0'(\boldsymbol{k}_1) & T^\dagger & \\ & T & h_0(\boldsymbol{k}_2) & g^\dagger(\boldsymbol{k}_2) \\ & & g(\boldsymbol{k}_2) & h_0'(\boldsymbol{k}_2) \end{pmatrix} + V, \tag{1}$$

and

$$H_{AB-BA}(\boldsymbol{k}) = \begin{pmatrix} h_0(\boldsymbol{k}_1) & g^\dagger(\boldsymbol{k}_1) & & \\ g(\boldsymbol{k}_1) & h_0'(\boldsymbol{k}_1) & T^\dagger & \\ & T & h_0'(\boldsymbol{k}_2) & g(\boldsymbol{k}_2) \\ & & g^\dagger(\boldsymbol{k}_2) & h_0(\boldsymbol{k}_2) \end{pmatrix} + V. \tag{2}$$

Here $\boldsymbol{k}_l = R(\pm\frac{\theta}{2})(\boldsymbol{k} - \boldsymbol{K}_\xi^l)$ is the in-plane momentum, with $R(\theta)$ being the two-dimensional rotation matrix and the sign $\pm$ for the top ($l = 1$) and bottom ($l = 2$) bilayer graphene, respectively. $\xi = \pm 1$ is the valley index and $\boldsymbol{K}_\xi^l$ is the corresponding Dirac point. Both $h_0(\boldsymbol{k})$ and $h_0'(\boldsymbol{k})$ describe the intralayer hoppings between sublattices A and B, while $g(\boldsymbol{k})$ denotes the coupling between the two layers in bilayer graphene. These 2×2 submatrices are written as

$$h_0(\boldsymbol{k}) = \begin{pmatrix} \Delta & -\gamma_0 f(\boldsymbol{k}) \\ -\gamma_0 f^*(\boldsymbol{k}) & 0 \end{pmatrix}, \tag{3}$$

$$h_0'(\boldsymbol{k}) = \begin{pmatrix} 0 & -\gamma_0 f(\boldsymbol{k}) \\ -\gamma_0 f^*(\boldsymbol{k}) & \Delta \end{pmatrix}, \tag{4}$$

$$g(\boldsymbol{k}) = \begin{pmatrix} \gamma_4 f(\boldsymbol{k}) & \gamma_3 f^*(\boldsymbol{k}) \\ \gamma_1 & \gamma_4 f(\boldsymbol{k}) \end{pmatrix}, \tag{5}$$

where γ_0 is the nearest-neighbor hopping integral and $f(\boldsymbol{k}) = \sum_i e^{-i\boldsymbol{k}\cdot\boldsymbol{\delta}_i}$, with $\boldsymbol{\delta}_1 = a_0(0, -\frac{1}{\sqrt{3}})$, $\boldsymbol{\delta}_2 = a_0(-\frac{1}{2}, \frac{1}{2\sqrt{3}})$, $\boldsymbol{\delta}_3 = a_0(\frac{1}{2}, \frac{1}{2\sqrt{3}})$ denoting the vectors pointing from sublattice A to B, and a_0 being the lattice constant. We can expand $f(\boldsymbol{k})$ around the Dirac points $\boldsymbol{K}_\pm = (\pm\frac{4\pi}{3a_0}, 0)$ as $f(\boldsymbol{K}_\pm + \boldsymbol{k}) = \frac{\sqrt{3}a_0}{2}(\mp k_x + ik_y)$. In $g(\boldsymbol{k})$, the parameter γ_3 represents the trigonal warping of the energy bands and γ_4 accounts for the electron-hole asymmetry in bilayer graphene [30]. The

tight-binding parameters are labeled in detail in Fig. 1. We use the parameters that are extracted from the *ab initio* results of Ref. [31], $\gamma_0 = 2610$ meV, $\gamma_1 = 361$ meV, $\gamma_3 = 283$ meV, $\gamma_4 = 138$ meV, and $\Delta = 15$ meV.

The term V in the Hamiltonian describes the effect of the out-of-plane perpendicular electric field, as it can induce the interlayer asymmetric electric potential. In bilayer graphene, the electric potential difference between the two layers can open a gap in the parabolic touching bands [30]. We assume that the electric potential drop between the neighboring layers is uniform, $U_i - U_{i+1} = \frac{U}{3}$, as shown in Fig. 1. Specifically,

$$V = \begin{pmatrix} \frac{U}{2}I & & & \\ & \frac{U}{6}I & & \\ & & -\frac{U}{6}I & \\ & & & -\frac{U}{2}I \end{pmatrix}, \tag{6}$$

with I being the 2×2 unit matrix. In the experiment, the electric potential in TDBG can be effectively tuned by the top and back gates [11–14].

The tunneling $T(\boldsymbol{r})$ between the top and bottom bilayer graphene varies with the moiré period and is written as [6,26]

$$T(\boldsymbol{r}) = T_0 + e^{-i\boldsymbol{b}_+\cdot\boldsymbol{r}}T_{+1} + e^{-i\boldsymbol{b}_-\cdot\boldsymbol{r}}T_{-1}, \tag{7}$$

$$T_j = w_0\sigma_0 + w_1\cos\left(j\frac{2\pi}{3}\right)\sigma_x + w_1\sin\left(j\frac{2\pi}{3}\right)\sigma_y, \tag{8}$$

where $\boldsymbol{b}_\pm = \frac{4\pi}{\sqrt{3}a_M}(\pm\frac{1}{2}, \frac{\sqrt{3}}{2})$ are the moiré reciprocal lattice vectors and $a_M = \frac{a_0}{2\sin\frac{\theta}{2}}$ denotes the moiré period. Because the moiré period is much larger than the lattice constant, $a_M \gg a_0$, the intervalley scatterings can be safely ignored and we treat the two valleys separately. Moreover, as the two valleys are connected by the TRS, we mainly focus on the $\boldsymbol{K}$ valley, while the physics of the $\boldsymbol{K}'$ valley can be obtained by the TR operation. w_0 and w_1 are the two tunneling parameters, which in general are unequal due to the layer corrugation in the moiré pattern. We take $w_0 = 79.5$ meV and $w_1 = 97.5$ meV [26] in the following calculations.

The moiré potential reconstructs the original Dirac linear bands into the small moiré Brillouin zone (MBZ). Numerically, the band structures can be effectively calculated by using the plane-wave expansions [6]. For each momentum $\boldsymbol{k}$, we use the basis that include the states of $(2M+1)\times(2M+1)$ momentum points: $\boldsymbol{k} + n_1\boldsymbol{b}_+ + n_2(\boldsymbol{b}_+ - \boldsymbol{b}_-)$, where $-M \leqslant n_1, n_2 \leqslant M$ are integers. In the calculations, we choose $M = 4$ to achieve results that are well convergent.

III. PHASE DIAGRAM

First we calculate the $\boldsymbol{K}$ valley Chern number phase diagram of TDBG, as the moiré bands are generically topological and can carry nonzero Chern number [10]. For the nth band, its Chern number is defined as an integration over the MBZ [32]

$$C_n = \frac{i}{2\pi}\int_{\mathrm{MBZ}} d^2\boldsymbol{k}\left\langle\frac{\partial u_{n\boldsymbol{k}}}{\partial\boldsymbol{k}}\right| \times \left|\frac{\partial u_{n\boldsymbol{k}}}{\partial\boldsymbol{k}}\right\rangle, \tag{9}$$

with $|u_{n\boldsymbol{k}}\rangle$ being the Bloch wave function. The Chern number can be numerically calculated by using the Fukui's algorithm, in which the BZ is divided into many disconnected sectors and a unique topological invariant is assigned to each sector. Then the Chern number is written as [33,34]

$$C_n = \frac{1}{2\pi}\sum_i \mathrm{Im}\big[\ln\big(\langle u^1_{n\boldsymbol{k}_i}|u^2_{n\boldsymbol{k}_i}\rangle\langle u^2_{n\boldsymbol{k}_i}|u^3_{n\boldsymbol{k}_i}\rangle \times \langle u^3_{n\boldsymbol{k}_i}|u^4_{n\boldsymbol{k}_i}\rangle\langle u^4_{n\boldsymbol{k}_i}|u^1_{n\boldsymbol{k}_i}\rangle\big)\big], \tag{10}$$

where the summation is to be taken over all disconnected sectors, and $|u^j_{n\boldsymbol{k}_i}\rangle$ ($j = 1, 2, 3, 4$ in anticlockwise direction) is the nth wave vector corresponding to the four vertices in the ith sector. The advantage of the Fukui's algorithm is that it can calculate the Chern number of a specific band in a reliable way, even when neighboring bands are overlapped, as long as the bands do not touch with each other. We label the Chern number of the nth valence (conduction) bands as C_{vn} (C_{cn}). The first valence and first conduction bands will be focused on and the Chern numbers (C_{v1}, C_{c1}) are used to distinguish the different phases, as they can undergo multiple changes at the high-symmetry points in the MBZ.

When the electric potential U in TDBG reverses its direction, we find that for AB-AB stacking, the Chern number of the nth band turns to its opposite value, $C_n(-U) = -C_n(U)$, while for AB-BA stacking, it will not change, $C_n(-U) = C_n(U)$. This is because in AB-AB stacking, the C_{2x} symmetry is broken by the electric potential, while in AB-BA stacking, the C_{2x} symmetry is maintained. Specifically, if we rotate the TDBG system with negative U by 180° along the x axis in the two-dimensional (2D) plane, for AB-AB stacking, the rotated system becomes BA-BA stacking with positive U. As the chirality of the massive bands changes, it makes the Chern number reverse to its opposite value. However, for AB-BA stacking, the rotated system returns to its origin with positive U and thus the Chern number remains unchanged. This property may be used in the experiment to judge whether the chiralities of the two stacked bilayer graphene are the same or not.

The $\boldsymbol{K}$-valley Chern number phase diagram of TDBG is plotted in Fig. 2 with AB-AB stacking in Fig. 2(a) and AB-BA stacking in Fig. 2(e), where the different phases are labeled in different colors. We can see that the Chern number are tunable up to ±3. Clearly, there are significant discrepancies of the two phase diagrams in the two stacking types. The typical moiré band structures along the high-symmetry line in the MBZ are plotted in Figs. 2(b) to 2(d) and Figs. 2(f) and 2(g). We define the band gap between the first conduction and second conduction band as δ_1, the band gap between the first conduction and valence band as δ_2, and the band gap between the first valence and second valence band as δ_3. When θ is small and U is lower than 20 meV, the first conduction and valence band touch with each other [e.g., see Fig. 2(b)], making δ_1 unopened and the Chern number ill-defined. However, the band gaps δ_1 and δ_3 are opened and can protect the sum of the Chern numbers. So we use $C_{c1} + C_{v1}$ to characterize these phases. As shown in Figs. 2(a) and 2(e), the phase of $C_{c1} + C_{v1} = 0$ and $C_{c1} + C_{v1} = 4$ spans the lower left region of the phase diagram, respectively.

For AB-AB stacking, when $U = 0$ and $\theta > 1°$, the two touching bands are separated. The increasing θ drives the system first enter the $(3, -3)$ phase and then the (0,0) phase [Fig. 2(c)]. As the two lowest bands are separated from the

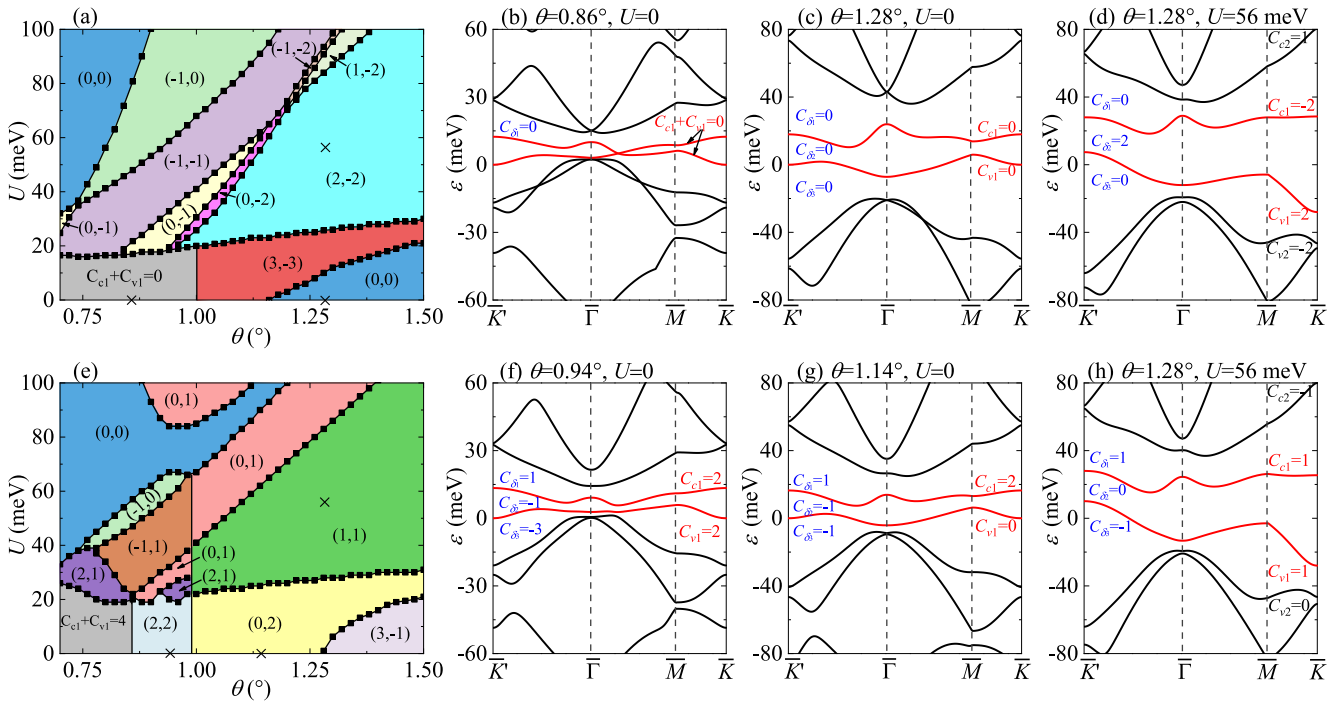

FIG. 2. The $\boldsymbol{K}$ valley Chern number phase diagram of TDBG in the parameter space (θ, U) with (a) AB-AB stacking and (e) AB-BA stacking. The different phases are characterized by the Chern numbers of the first valence and conduction band (C_{v1}, C_{c1}). (b)–(d) and (f)–(h) are the typical moiré bands along the high-symmetry line, $\bar{K}' \to \bar{\Gamma} \to \bar{M} \to \bar{K}$, in the MBZ, with the parameter points being marked by the crosses in (a) and (e), respectively. Note that Chern numbers are labeled in each figure.

higher bands, the summation of the Chern numbers remains zero, $C_{c1} + C_{v1} = 0$. We can see that the Chern number in the middle band gap, C_{δ_2}, which is defined as the summation of the band Chern number below the band gap δ_2, is also zero. The increasing U can drive the bands touch at the high-symmetry points and then separate, resulting in the change of C_{c1} or C_{v1}. Note that the $(2, -2)$ phase [Fig. 2(d)] spans a broad parameter region in the phase diagram, meaning that it remains unchanged to the small variations of U and θ. Moreover, the $(2, -2)$ phase represents a valley Chern insulator as $C_{\delta_2} = 2$.

For AB-BA stacking, when $U = 0$ and $0.86^\circ < \theta < 0.98^\circ$, the Chern numbers become (2,2), but the direct gap is too small or even does not exist [Fig. 2(f)]. When $U < 66$ meV and $\theta \sim 0.98^\circ$, the first valence band will touch with the higher valence band at the $\bar{\Gamma}$ point. Thus the phase transitions happen and a vertical phase boundary at $\theta \sim 0.98^\circ$ is seen, where C_{v1} varies but C_{c1} remains unchanged. For example, at $U = 0$, the increasing θ drives the (2,2) phase enter the (0,2) phase [Fig. 2(g)]. It shows that $C_{\delta_2} = -1$ and is distinct from AB-AB stacking. We also note that the (1,1) [Fig. 2(h)] phase behaves as a trivial insulator as $C_{\delta_2} = 0$. More importantly, it spans a similar broad parameter region in the phase diagram as the $(2, -2)$ phase in AB-AB stacking.

In a previous work [29], the valley Chern number phase diagrams of TDBG were obtained from the TKNN formula [see Eq. (11) below], which partly agreement with our results. The differences between them mainly lie in the parameter regions where the neighboring bands related to the first conduction and first valence bands are overlapped (see Appendix A). Our results show that when the neighboring bands are overlapped, the different computational methods may lead to different results (see Appendix B). As is known, when there is a direct band gap between the neighboring topological bands and the Fermi energy lies in it, the TKNN formula [see Eq. (12) below] can express the anomalous Hall conductivity (AHC) σ_H (in unit of $\frac{e^2}{h}$) as a quantized value, which equals the Chern number in the gap C_δ. Then the band Chern number is determined and equals the Chern number in the above band gap minus the Chern number in the below band gap. In this case, we checked that the Chern number results obtained by using the Fukui's algorithm and the TKNN formula are consistent with each other. When the the bands overlap, the quantized σ_H will not appear. In this case, the Chern number judgment from the TKNN formula may be inconvenient. However, we suggest that the Fukui's algorithm is still valid for determining the Chern number, as long as the neighboring bands do not touch each other. The valley Chern number phase diagram was also reported in another work [27], but was only about the first conduction band C_{c_1}. It is worth pointing out that our phase diagrams are also consistent with two recent studies [28,35], where the Chern numbers in TDBG are presented for some specific parameter points of (θ, U).

We further study the evolution of the first conduction band with the electric potential U, as it can be well isolated from other bands. In Fig. 3 with the fixed $\theta = 1.28^\circ$, we plot the flatness of the first conduction band w, the band gaps δ_1 and δ_2 as functions of U. It shows that for both AB-AB and AB-BA stacking types, these quantities exhibit similar trends. Around $U = 30$ meV, we have $w = 12.5$ meV, which

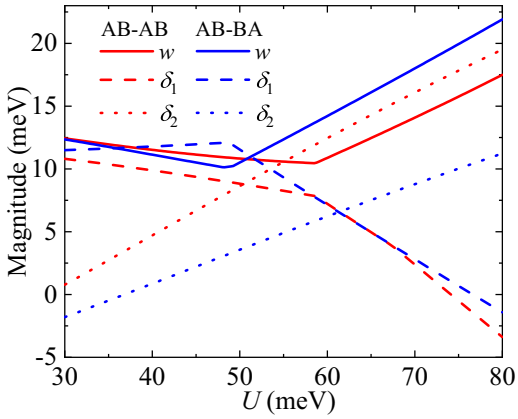

FIG. 3. The flatness w of the first conduction band, the gaps δ_1 and δ_2 vs the interlayer potential U in TDBG, where both AB-AB stacking and AB-BA stacking are considered. We set the twist angle $\theta = 1.28^\circ$.

is comparable to δ_1, whereas δ_2 is close to zero. At large U, both w and δ_2 increase while δ_1 decreases, meaning that the first conduction band becomes wider and moves closer to the second conduction band. In the extremal case when U is sufficiently high (low), the neighboring bands overlap and δ_1 (δ_2) becomes negative. These results can be used to explain the recent resistance measurements in TDBG with θ being around 1.3° [13–15], where the insulating state at charge neutrality (corresponding to δ_2) strengthens with the electric potential U, while the $n = +n_s$ insulating state (corresponding to δ_1) is weakened and eventually disappears with the increasing U. In addition, the observed asymmetric change of insulating states at $n = +n_s$ and $n = -n_s$ versus U [13–15] can be attributed to the broken electron-hole symmetry in the TDBG moiré bands.

IV. ORBITAL CHERN INSULATOR

As the strong electron-electron interactions exist in the flat bands, the four-fold degeneracy of each moiré band may be spontaneously broken by the interaction-induced spin-splitting Δ_s and valley-splitting Δ_v. To study the effect of interaction, we phenomenologically introduce Δ_s and Δ_v in the TDBG system, with the Hamiltonian [23,27,35,36]

$$H_{sv} = \Delta_s s_z + \Delta_v \tau_z. \tag{11}$$

Here s_z and τ_z both denote the third Pauli matrice, but are defined in the spin and valley subspace, respectively. In Fig. 4, with the electric potential $U = 56$ meV and the twist angle $\theta = 1.28^\circ$, we plot the splitted moiré bands and the corresponding density of states (DOS) in AB-AB stacking for a set of the splittings (Δ_s, Δ_v). The dotted horizontal line denotes the Fermi energy position at half-filling $n = \frac{1}{2}n_s$ of the first conduction band. Note that $w = 10.54$ meV.

Four cases are considered. (i) When $\Delta_s = \Delta_v = 0$, the four-fold degeneracy of the first conduction band is preserved [Fig. 4(a)], so the Fermi energy at half-filling lies in the band interior. As $\boldsymbol{K}$ and $\boldsymbol{K}'$ valleys are connected by the TRS, they have the same DOS and thus the total DOS is four times the DOS of one flavor [Fig. 4(b)]. (ii) When $\Delta_s = 0$ and $\Delta_v = 6$ meV, the bands are spin-degenerate but valley-splitted [Fig. 4(c)], so the total DOS evolves into two peaks [Fig. 4(d)]. At half-filling, we can see that a gap is opened and the system is valley polarized, with the first conduction bands

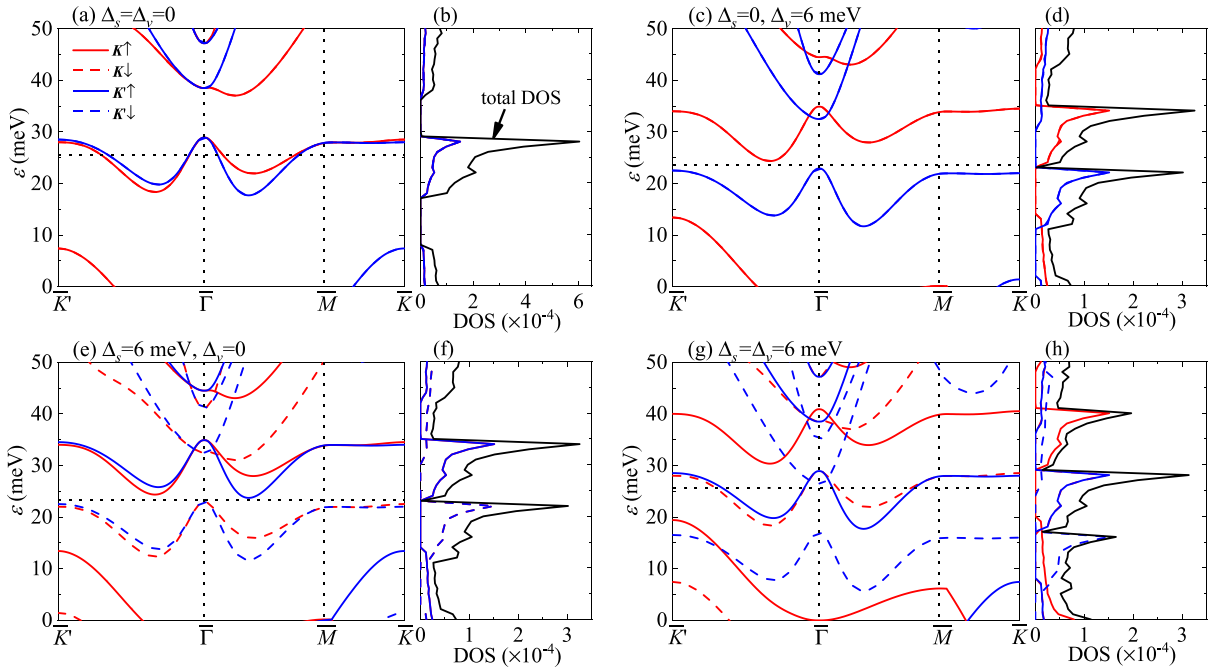

FIG. 4. The moiré bands (a), (c), (e), and (g), and the DOS (b), (d), (f), and (h) of TDBG with AB-AB stacking, with the different spin splitting Δ_s and valley splitting Δ_v. The band structures are along the high-symmetry line in the MBZ. The dotted horizontal line denotes the Fermi energy at half-filling of the first conduction band. We choose the parameters as $U = 56$ meV and $\theta = 1.28^\circ$. The legends are the same in all figures.

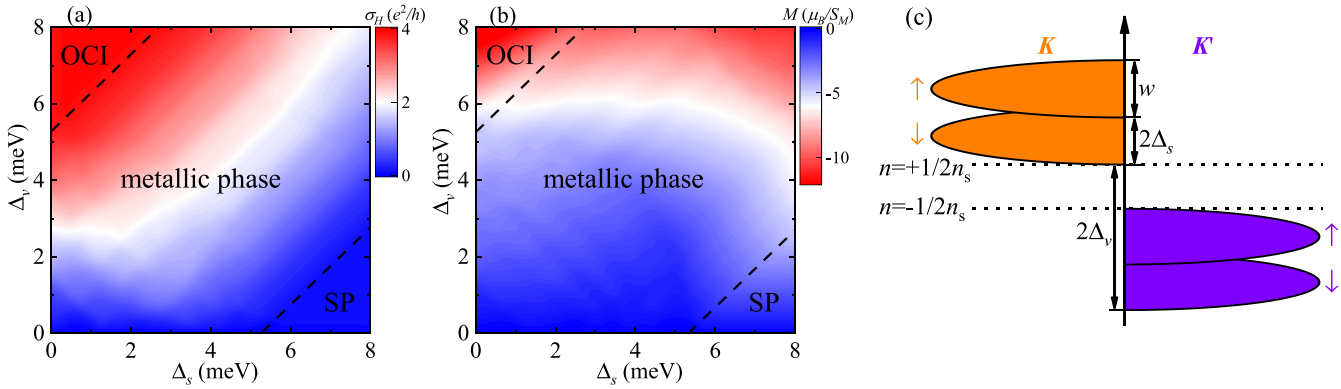

FIG. 5. The (a) AHC σ_H and (b) OM M of TDBG in the parametric space of the splittings (Δ_s, Δ_v) with AB-AB stacking. The dashed lines denote the phase boundaries, separating three phases: OCI phase, metallic phase, and SP phase. The Fermi energy is pinned at half-filling of the first conduction band. If a gap is opened at the half-filling, the Fermi energy is chosen to lie at the bottom of the gap. The parameters are taken as $U = 56$ meV and $\theta = 1.28°$. (c) The schematics of the valley-splitted and spin-splitted moiré bands. The Fermi energy positions at $n = \pm\frac{1}{2}n_s$ filling are denoted by the dotted lines.

in $\boldsymbol{K}'$ valley being completely filled while those in $\boldsymbol{K}$ valley being empty. Since the TRS has been broken by Δ_v, the AHE would occur in this case. (iii) When $\Delta_s = 6$ meV and $\Delta_v = 0$, the spin degeneracy is broken, with the upspin bands moving upwards and downspin bands moving downwards [Fig. 4(e)]. At half-filling, a gap is also opened and the system represents a spin-polarized (SP) state. In the experiment, by evaluating the g factor to be around $g \simeq 2$, the observed insulating phase at half-filling was attributed to this state, where the insulating gap is further enhanced by an in-plane magnetic field [13–15]. (iv) When $\Delta_s = \Delta_v = 6$ meV, both the spin and valley degeneracies are broken. At half-filling, there is no gap opening and the Fermi energy also lies in the band interior [Fig. 4(g)]. Because there is an overlap of the DOS of the $\boldsymbol{K}$ valley, downspin band and the $\boldsymbol{K}'$ valley, upspin band, the total DOS exhibits three peaks [Fig. 4(h)].

Normally, when both the splittings are larger than the moiré band flatness, gaps may be opened at the odd-fillings, $n = \frac{1}{4}n_s$ or $\frac{3}{4}n_s$. This is just the case in TBG, where the OCI phase with $C = 1$ was successfully observed in the $n = \frac{3}{4}n_s$ filling gap [4,5]. However, in TDBG, the flatness of the first conduction band may be large and can reach $10 \sim 30$ meV in the region that we focus on [see Appendix A]. This may lead to the closing of the gaps at odd-fillings, as the higher bands may move into the gap by the splittings. For example, in Fig. 4(g), the second conduction band of $\boldsymbol{K}'$ valley, downspin flavor moves downwards into the $n = \frac{3}{4}n_s$ gap and the first valence band of $\boldsymbol{K}$ valley, upspin flavor moves upwards into the $n = \frac{1}{4}n_s$ gap. These results agree well with the experiments [13–15], in which there is no insulating state observed at $n = \frac{3}{4}n_s$ filling gap, while the insulating state at $n = \frac{1}{4}n_s$ filling gap quickly disappears at the temperature less than 3 K [13], demonstrating that the gap is very small. According to these analyses, we suggest that the nontrivial Chern insulator phase in TDBG may only appear at half-filling $n = \frac{1}{2}n_s$ of the first conduction band when the condition $\Delta_v > \frac{1}{2}w + \Delta_s$ is satisfied, corresponding to the case of Fig. 4(c).

Next we study the dependence of the AHC and OM on the splittings, Δ_s and Δ_v. The AHC σ_H is calculated by the famous TKNN formula, which expresses σ_H as an integration of the Berry curvature over the MBZ [37],

$$\sigma_H = -\frac{e^2}{\hbar}\mathrm{Im}\int_{\mathrm{MBZ}}\frac{d^2\boldsymbol{k}}{(2\pi)^2}\sum_{n,n'\neq n} \times \frac{\langle u_{n\boldsymbol{k}}|\frac{\partial H}{\partial k_x}|u_{n'\boldsymbol{k}}\rangle\langle u_{n'\boldsymbol{k}}|\frac{\partial H}{\partial k_y}|u_{n\boldsymbol{k}}\rangle}{(\varepsilon_{n\boldsymbol{k}}-\varepsilon_{n'\boldsymbol{k}})^2} f(\varepsilon_F-\varepsilon_{n\boldsymbol{k}}), \quad (12)$$

and the OM M is calculated as [32,38,39]

$$M = \frac{e}{\hbar}\mathrm{Im}\int_{\mathrm{MBZ}}\frac{d^2\boldsymbol{k}}{(2\pi)^2}\sum_{n,n'\neq n}(\varepsilon_{n\boldsymbol{k}}+\varepsilon_{n'\boldsymbol{k}}-2\varepsilon_F) \times \frac{\langle u_{n\boldsymbol{k}}|\frac{\partial H}{\partial k_x}|u_{n'\boldsymbol{k}}\rangle\langle u_{n'\boldsymbol{k}}|\frac{\partial H}{\partial k_y}|u_{n\boldsymbol{k}}\rangle}{(\varepsilon_{n\boldsymbol{k}}-\varepsilon_{n'\boldsymbol{k}})^2} f(\varepsilon_F-\varepsilon_{n\boldsymbol{k}}), \quad (13)$$

where $f(\varepsilon_F - \varepsilon_{n\boldsymbol{k}})$ is the Fermi-Dirac distribution function and ε_F is the Fermi energy. We use $\frac{e^2}{\hbar}$ and $\frac{\mu_B}{S_M}$ as the unit of σ_H and M, respectively, with μ_B being the Bohr magneton. The OM can be separated into two parts $M = M_1 + M_2$ [23],

$$M_1 = \frac{e}{\hbar}\mathrm{Im}\int_{\mathrm{MBZ}}\frac{d^2\boldsymbol{k}}{(2\pi)^2}\sum_{n,n'\neq n}(\varepsilon_{n\boldsymbol{k}}+\varepsilon_{n'\boldsymbol{k}}) \times \frac{\langle u_{n\boldsymbol{k}}|\frac{\partial H}{\partial k_x}|u_{n'\boldsymbol{k}}\rangle\langle u_{n'\boldsymbol{k}}|\frac{\partial H}{\partial k_y}|u_{n\boldsymbol{k}}\rangle}{(\varepsilon_{n\boldsymbol{k}}-\varepsilon_{n'\boldsymbol{k}})^2} f(\varepsilon_F-\varepsilon_{n\boldsymbol{k}}), \quad (14)$$

and

$$M_2 = \frac{e}{\hbar}\mathrm{Im}\int_{\mathrm{MBZ}}\frac{d^2\boldsymbol{k}}{(2\pi)^2}\sum_{n,n'\neq n}(-2\varepsilon_F) \times \frac{\langle u_{n\boldsymbol{k}}|\frac{\partial H}{\partial k_x}|u_{n'\boldsymbol{k}}\rangle\langle u_{n'\boldsymbol{k}}|\frac{\partial H}{\partial k_y}|u_{n\boldsymbol{k}}\rangle}{(\varepsilon_{n\boldsymbol{k}}-\varepsilon_{n'\boldsymbol{k}})^2} f(\varepsilon_F-\varepsilon_{n\boldsymbol{k}}). \quad (15)$$

The above equations show that when the Fermi energy ε_F lies in the gap, M_1 is independent of ε_F, while M_2 exhibits a linear dependence on ε_F. In particular, M_2 is closely related to the edge states as its coefficient is proportional to the Chern number in the gap, $\frac{dM_2}{d\varepsilon_F} = \frac{e}{2\pi\hbar}C_\delta$.

We show the AHC σ_H and OM M of AB-AB stacking in Figs. 5(a) and 5(b), respectively. The splittings Δ_s and Δ_v

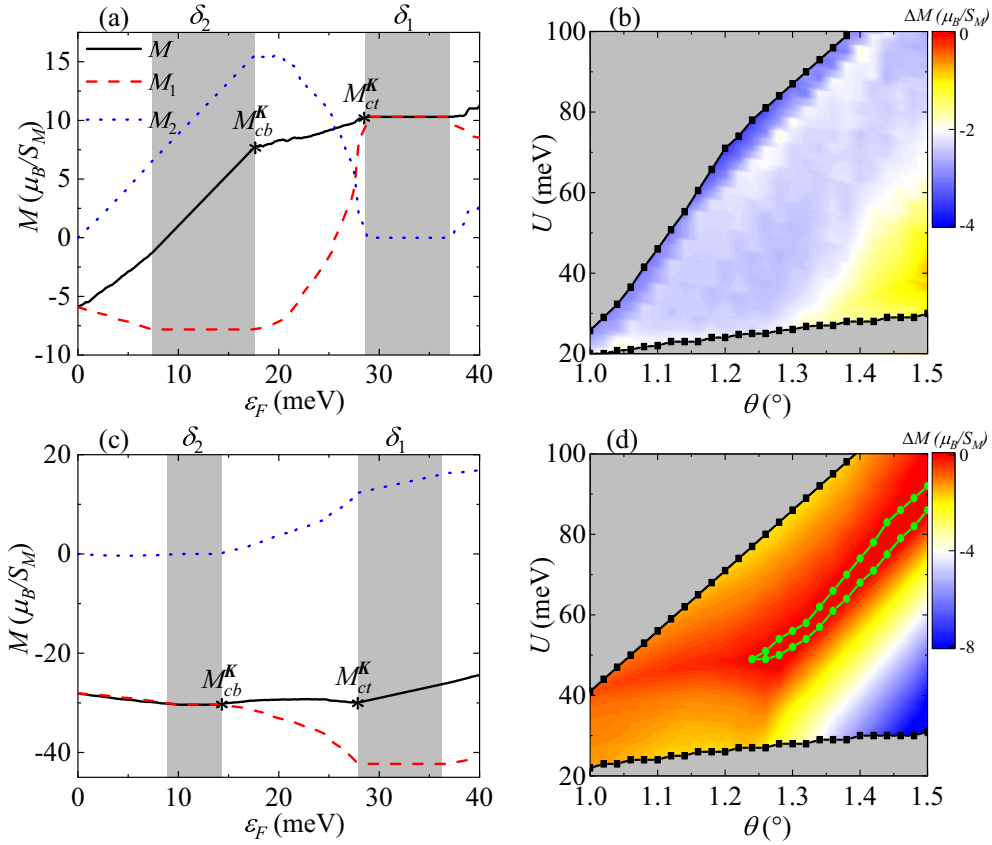

FIG. 6. The single-flavor OM M in $\boldsymbol{K}$ valley and $\Delta M = M^{\boldsymbol{K}}_{cb} - M^{\boldsymbol{K}}_{ct}$ of TDBG with (a, b) AB-AB stacking and (c, d) AB-BA stacking. In (a) and (c), the parameters are taken as $U = 56$ meV and $\theta = 1.28^\circ$. The red dashed and blue dotted lines denote M_1 and M_2, respectively. The gray stripes indicate the energy gaps δ_1 and δ_2. The extremal OMs $M^{\boldsymbol{K}}_{cb}$ and $M^{\boldsymbol{K}}_{ct}$ are marked by the asterisks. In (b) and (d), we focus on the $(2, -2)$ phase and (1,1) phase, respectively, while the gray areas are outside of the $(2, -2)$ and (1,1) phase. Both figures show that ΔM is negative, except that in a small region of (d), as highlighted by the green lines, ΔM is positive, but can reach $\sim 0.1\frac{\mu_B}{S_M}$ at most.

are varied from 0 to 8 meV. The Fermi energy is pinned at half-filling of the first conduction band. If a gap is opened at half-filling, the Fermi energy is chosen to lie at the bottom of the gap. We can see that when $\Delta_v = 0$ and the TRS is preserved, both σ_H and M vanish due to the opposite contributions from the $\boldsymbol{K}$ and $\boldsymbol{K}'$ valleys. For a fixed Δ_s, when Δ_v increases, more electronic states in $\boldsymbol{K}'$ valley than $\boldsymbol{K}$ valley are occupied. Correspondingly, σ_H increases from zero, while M decreases from zero to a large negative value.

Three phases that are separated by the dashed lines can be seen in Fig. 5. Above the phase boundary $\Delta_v = \frac{1}{2}w + \Delta_s$, a gap is opened at half-filling $n = \frac{1}{2}n_s$ of the first conduction band and the system enters the OCI phase. Because both the occupied upspin and downspin band in $\boldsymbol{K}'$ valley have the Chern number $C^{\boldsymbol{K}'}_{c1} = 2$ (opposite to $C^{\boldsymbol{K}}_{c1} = -2$), σ_H is quantized as $4\frac{e^2}{h}$, as shown in Fig. 5(a). But M will further decrease with Δ_v due to the contributions from the edge states in the gap, as in Fig. 5(b). As the upspin and downspin states are equally occupied in the OCI phase, the spin magnetization vanishes and therefore the total magnetization is dominated by the orbital component. When $\Delta_v = 8$ meV and Δ_s increases, σ_H gradually deviates from the quantized value, whereas M is still large and around $-10\frac{\mu_B}{S_M}$. On the other hand, below the phase boundary $\Delta_s = \frac{1}{2}w + \Delta_v$, a gap is also opened at half-filling of the first conduction band and the system enters the SP ferromagnetic state. As the TRS is unbroken ($\Delta_v = 0$) or weakly broken ($\Delta_v \ll w$), σ_H is zero or vanishingly small, while M gives a small value, which also originates from the edge states in the gap. Between the phase boundaries, a metallic phase is present in the parameter space due to the finite DOS at the Fermi energy. We note that the exact positions of the phase boundaries are dependent on the electric potential U and the twist angle θ, as the flatness w can be effectively modulated (see Appendix A). Although only AB-AB stacking is considered in Figs. 4 and 5, similar conclusions can also be obtained for AB-BA stacking, except that the AHC would be quantized as $\sigma_H = -2\frac{e^2}{h}$ for the same U and θ.

We further explore whether there is a OM reversal in the half-filling gap of TDBG when the OCI phase has been identified. To see the behavior of the OM M, in Fig. 6, we plot the single-flavor M in $\boldsymbol{K}$ valley (no splittings) as a function of the Fermi energy ε_F with AB-AB stacking [Fig. 6(a)] and AB-BA stacking [Fig. 6(c)] when the parameters $U = 56$ meV and $\theta = 1.28^\circ$. The red dashed and blue dotted lines denote the separated M_1 and M_2 contributions, respectively. As $\boldsymbol{K}$ and $\boldsymbol{K}'$ valleys are TR counterparts, their OM contributions

are opposite in sign. In Fig. 6(a), we observe that M in $\boldsymbol{K}$ valley keeps unchanged in δ_1 gap as the Chern number $C^{\boldsymbol{K}}_{\delta_1}=0$, and increases linearly in δ_2 gap as $C^{\boldsymbol{K}}_{\delta_2}=2$, while in Fig. 6(c), M in $\boldsymbol{K}$ valley increases linearly in δ_1 gap as $C^{\boldsymbol{K}}_{\delta_1}=1$ and remains unchanged in δ_2 gap as $C^{\boldsymbol{K}}_{\delta_2}=0$. Note that, due to the absence of the electron-hole symmetry in TDBG, M does not vanish at zero Fermi energy. This is in sharp contrast with TBG, where the electron-hole symmetry is well preserved and M always vanishes at zero Fermi energy [23].

When the splittings are present in TDBG, the total OMs require to sum over all spin and valley flavors. For the OCI at $n=\pm\frac{1}{2}n_s$ filling, with the Fermi energy positions being denoted by the dotted lines in Fig. 5(c), the OM in each flavor can be easily obtained. For example, we have $M^{\boldsymbol{K}\uparrow}_{+\frac{1}{2}n_s}=M^{\boldsymbol{K}}_{cb}-\frac{e}{2\pi\hbar}C^{\boldsymbol{K}}_{\delta_2}2\Delta_s$ and $M^{\boldsymbol{K}\uparrow}_{-\frac{1}{2}n_s}=M^{\boldsymbol{K}}_{cb}-\frac{e}{2\pi\hbar}C^{\boldsymbol{K}}_{\delta_2}(2\Delta_v-w)$.

For AB-AB stacking, the total OMs are

$$M_{+\frac{1}{2}n_s}=2\Delta M-\frac{e}{\pi\hbar}C^{\boldsymbol{K}}_{\delta_2}\Delta_s, \tag{16}$$

$$M_{-\frac{1}{2}n_s}=2\Delta M-\frac{e}{\pi\hbar}C^{\boldsymbol{K}}_{\delta_2}(2\Delta_v-\Delta_s-w), \tag{17}$$

where $\Delta M=M^{\boldsymbol{K}}_{cb}-M^{\boldsymbol{K}}_{ct}$, with $M^{\boldsymbol{K}}_{cb}$ and $M^{\boldsymbol{K}}_{ct}$ denoting the extremal OM with the Fermi energy being located at the band bottom and top, respectively. Eq. (17) tells us that $M_{-\frac{1}{2}n_s}$ decreases with Δ_v, but increases with Δ_s, as observed in the top left of Fig. 5(b). The difference between $M_{+\frac{1}{2}n_s}$ and $M_{-\frac{1}{2}n_s}$ is

$$M_{+\frac{1}{2}n_s}-M_{-\frac{1}{2}n_s}=\frac{e}{\pi\hbar}C^{\boldsymbol{K}}_{\delta_2}(2\Delta_v-2\Delta_s-w), \tag{18}$$

which is positive when taking into account the condition for the OCI, $\Delta_v>\frac{1}{2}w+\Delta_s$. In Fig. 6(a), we can see that $0<M^{\boldsymbol{K}}_{cb}<M^{\boldsymbol{K}}_{ct}$ and thus $M_{-\frac{1}{2}n_s}<M_{+\frac{1}{2}n_s}<0$. This means that the OM will increase from the bottom to the top of the half-filling gap, but remains negative. We further check this in the whole $(2,-2)$ phase. As the total OMs depend heavily on ΔM, we plot ΔM in Fig. 6(b), where ΔM is always negative, indicating that there is no OM reversal in AB-AB stacking.

For AB-BA stacking, the total OMs are

$$M_{+\frac{1}{2}n_s}=2\Delta M-\frac{e}{\pi\hbar}C^{\boldsymbol{K}}_{\delta_1}(2\Delta_v-\Delta_s-w), \tag{19}$$

$$M_{-\frac{1}{2}n_s}=2\Delta M-\frac{e}{\pi\hbar}C^{\boldsymbol{K}}_{\delta_1}\Delta_s. \tag{20}$$

Their difference is

$$M_{+\frac{1}{2}n_s}-M_{-\frac{1}{2}n_s}=-\frac{e}{\pi\hbar}C^{\boldsymbol{K}}_{\delta_1}(2\Delta_v-2\Delta_s-w), \tag{21}$$

which is negative for the OCI state. Figure 6(c) shows that $M^{\boldsymbol{K}}_{cb}<M^{\boldsymbol{K}}_{ct}<0$, so we can identify that $M_{+\frac{1}{2}n_s}<M_{-\frac{1}{2}n_s}<0$, meaning that the OM will decrease from the bottom to the top of the half-filling gap, but again remains negative. In Fig. 6(d), we also check ΔM in the whole (1,1) phase. It shows that ΔM is mostly negative, except for a small region where ΔM becomes positive, as has been highlighted by the green lines. However, in this region, ΔM can only reach $\sim 0.1\frac{\mu_B}{S_M}$ at most. Considering that $\frac{e\cdot\mathrm{meV}}{\pi\hbar}=0.884\frac{\mu_B}{S_M}$ and $2\Delta_v-\Delta_s-w>\Delta_s$, a sufficiently weak $\Delta_s\sim 0.23$ meV can make $M_{\pm\frac{1}{2}n_s}$ remain negative. Thus we suggest that the OMs are also negative and there is no OM reversal in AB-BA stacking.

In Ref. [23], by studying the magnetic property in TBG, the authors expected that the sign reversal of the OM is common in the large gap OCI. Here we demonstrated that this conclusion does not hold in the OCI state of TDBG, which may be attributed to the specific band topologies in TDBG. So the necessary conditions for the OM reversal in the OCI state based on the moiré flat-band systems need more investigation.

V. DISCUSSIONS AND SUMMARIES

When comparing with the experiments [13–15], we find that the typical electric potential performed on TDBG is higher than that used in our theoretical calculations. This may be attributed to the fact that in our model, the uniform electric potential drop is assumed between neighboring layers, but in real samples, the uniform electric potential drop cannot exist because the separation between the double bilayer graphene is evidently larger than the separation between the two layers of one bilayer graphene. Nevertheless, the effect of the electric potential in TDBG can still be qualitatively captured by the theoretical model.

We make some comparisons of the topological moiré bands between TBG and TDBG. In TBG, the observation of the flat moiré bands needs to fix the twist angle to the specific magic angle, $\theta\sim 1.1^\circ$. The nontrivial band topology requires to perfectly align the TBG system with the hexagonal boron nitride cladding layers [5,40,41], as to break the C_{2z} symmetry between the two sublattices and acquire a finite mass for the Dirac cone. These conditions are rather strict constraints in the experiment. Here in TDBG, the flat bands can exist in a large twist-angle range, as is shown in the phase diagrams and has been demonstrated in the experiment [13–15]. Because both the twist angle and electric potential can be controlled in experiment, this makes the band Chern number in TDBG be effectively modulated.

In summary, in this paper, we investigated the phase diagram and OCI in TDBG modulated by the twist angle and the electric field. As the stacking type plays an important role in determining the band topology of TDBG, we find that it can be inferred by judging the valley Chern number with the reversed direction of the electric potential. The appearance of the OCI in TDBG requires the strong valley splitting to open a gap at half-filling of the first conduction band. The experiments [13–15] and the Hatree-Fock calculations [27] pointed to the SP state at half-filling due to the strong spin splittings by the correlation effect. Therefore the realization of the strong valley splitting in TDBG may require more delicate conditions, which need more theoretical and experimental studies in the future.

ACKNOWLEDGMENTS

This work was supported by NSFC (Grants No. 11704157, No. 11804122, and No. 11905054), and the Fundamental Research Funds for the Central Universities of China.

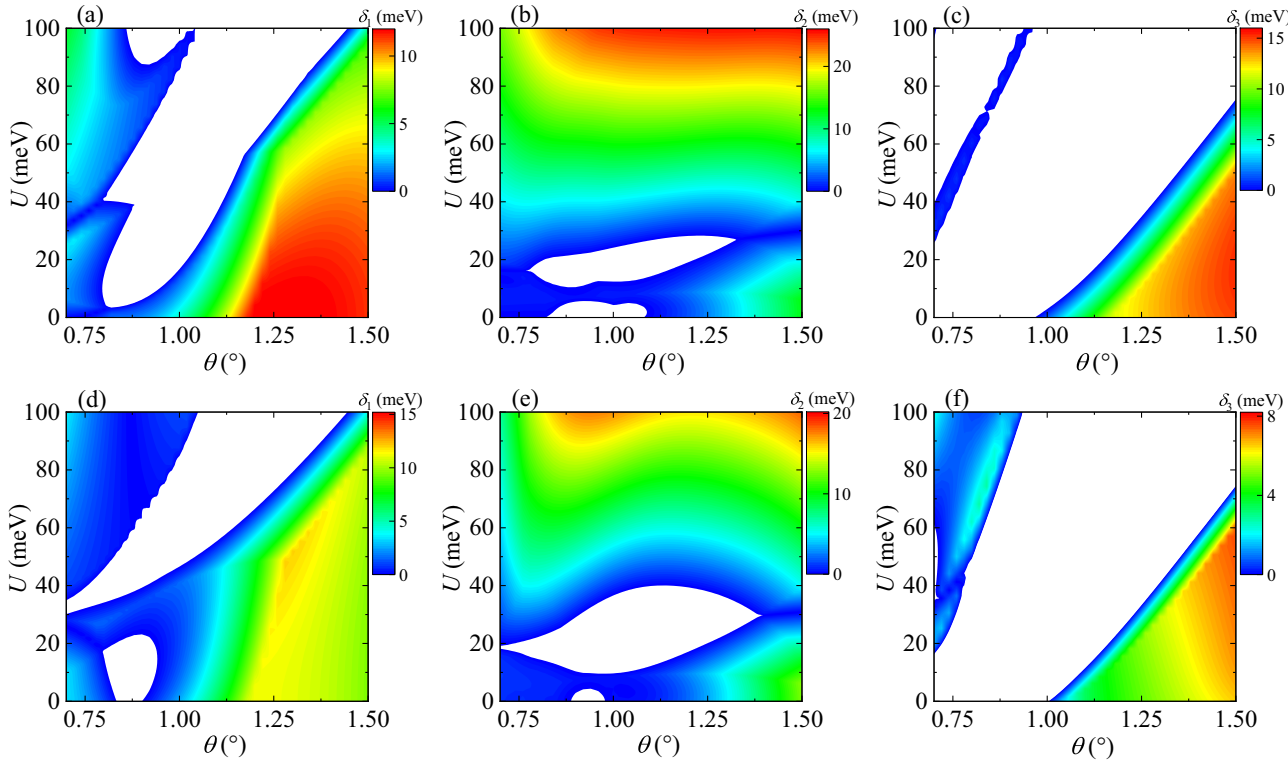

FIG. 7. The band gaps δ_1, δ_2, and δ_3 of TDBG in the parametric space (θ, U) with (a)–(c) AB-AB stacking and (d)–(f) AB-BA stacking. δ_1 is the band gap between the first conduction and second conduction band, δ_2 is the band gap between the first conduction and valence band, and δ_3 is the band gap between the first valence and second valence band.

APPENDIX A: BAND GAPS AND FLATNESS

We calculate the band gaps δ_1, δ_2, and δ_3 of TDBG, which are defined as

$$\delta_1 = \min(\varepsilon_{2c}) - \max(\varepsilon_{1c}), \tag{A1}$$

$$\delta_2 = \min(\varepsilon_{1c}) - \max(\varepsilon_{1v}), \tag{A2}$$

$$\delta_3 = \min(\varepsilon_{1v}) - \max(\varepsilon_{2v}), \tag{A3}$$

and the flatness of the first conduction band

$$w = \max(\varepsilon_{1c}) - \min(\varepsilon_{1c}). \tag{A4}$$

In Fig. 7, the contour plots of the band gaps are presented. When the neighboring bands are overlapped, there is no direct band-gap opening and the band gap becomes negative. We can see that the regions for the overlapped bands are roughly the same for AB-AB stacking and AB-BA stacking. Note that for AB-AB stacking, the obtained band-gap results are consistent with those in Figs. 7(a) to 7(c) of Ref. [27]. For δ_2, the regions

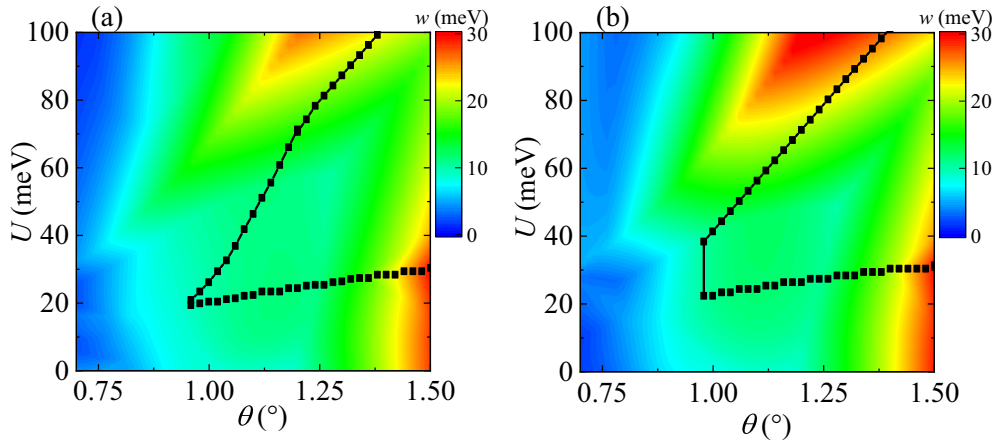

FIG. 8. The flatness w of the first conduction band of TDBG in the parametric space (θ, U) with (a) AB-AB stacking and (b) AB-BA stacking. The regions that we focus on the OCI are inside of the black lines in each figure.

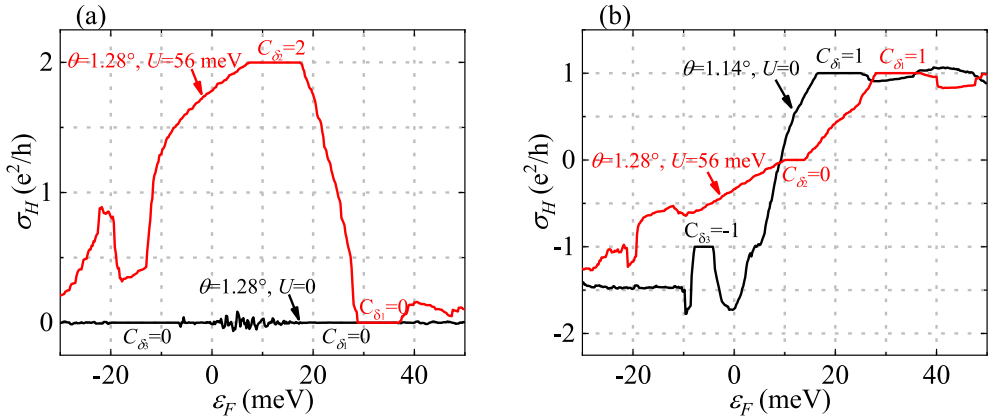

FIG. 9. The AHC σ_H (in units of $\frac{e^2}{h}$) calculated by using the TKNN formula [Eq. (12)], with the parameters in (a) and (b) being the same as those in Figs. 2(c) and 2(d) and Figs. 2(g) and 2(h), respectively. When the neighboring bands are overlapped, σ_H will not be quantized, as in both (a) and (b), there is no C_{δ_3} plateau of the red line and no C_{δ_2} plateau of the black line.

appear in the bottom with low U [Figs. 7(b) and 7(e)], while for δ_1 and δ_3, the overlapped bands can span quite a large region in the parametric space [Figs. 7(a), 7(c) 7(d), and 7(f)]. Thus we arrive at the conclusion that the overlapped bands related to the first conduction and first valence bands are quite common for the small twist-angle TDBG modulated by the electric potential.

In Fig. 8, the contour plots of the flatness are presented. The regions that we focus on the OCI, the $(2, -2)$ phase in Fig. 8(a) and (1,1) phase in Fig. 8(b), are inside the black lines. We can see that in these regions, the flatness w can reach 10–30 meV, ensuring that the band gap cannot be opened at the odd fillings, $n = \frac{1}{4}n_s$ or $n = \frac{3}{4}n_s$, by the splittings.

APPENDIX B: CHERN NUMBER DETERMINATION FROM THE TKNN FORMULA

By using the TKNN formula [Eq. (12)], the AHC σ_H of the system can be calculated as a function of the Fermi energy ε_F. In Fig. 9, we plot the calculated σ_H, with the parameters in Figs. 9(a) and 9(b) chosen to be the same as those in Figs. 2(c) and 2(d) and 2(g) and 2(h), respectively.

Comparing the Chern number determination from the TKNN formula and Fukui's algorithm, we can see that when the direct gap dominates the system, the results are the same. But when the neighboring bands are overlapped, the results are different, as σ_H will not be quantized in the TKNN formula. This is clearly seen in both Figs. 9(a) and 9(b), where there is no C_{δ_3} plateau of the red line and no C_{δ_2} plateau of the black line.

For example, in Fig. 9(a) of the red line, with $\theta = 1.28^\circ$ and $U = 56$ meV, we observe that $C_{\delta_1} = 0$ and $C_{\delta_2} = 2$. Then the Chern number of the first conduction band is determined as $C_{c1} = C_{\delta_1} - C_{\delta_2} = -2$. This Chern number value is consistent with that obtained from the Fukui's algorithm, as labeled in Fig. 2(d). On the other hand, when the negative δ_3 gap is present that the first valence and second valence bands are overlapped, which is evidently seen in the moiré band structure in Fig. 2(d), no quantized σ_H is observed. Consequently, the Chern number of the first valence band C_{v1} is not well judged from the TKNN formula. Similar cases can also be seen in other lines of Fig. 9. However, even with the presence of the overlapped bands, we suggest that the Chern number can still be well determined from the Fukui's algorithm, as long as the neighboring moiré bands do not touch each other.

[1] Y. Cao, V. Fatemi, A. Demir, S. Fang, S. L. Tomarken, J. Y. Luo, J. D. Sanchez-Yamagishi, K. Watanabe, T. Taniguchi, E. Kaxiras, R. C. Ashoori, and P. J. Herrero, Nature (London) **556**, 80 (2018).

[2] Y. Cao, V. Fatemi, S. Fang, K. Watanabe, T. Taniguchi, E. Kaxiras, and P. J. Herrero, Nature (London) **556**, 43 (2018).

[3] M. Yankowitz, S. Chen, H. Polshyn, Y. Zhang, K. Watanabe, T. Taniguchi, D. Graf, A. F. Young, and C. R. Dean, Science **363**, 1059 (2019).

[4] A. L. Sharpe, E. J. Fox, A. W. Barnard, J. Finney, K. Watanabe, T. Taniguchi, M. A. Kastner, and D. G. Gordon, Science **365**, 608 (2019).

[5] M. Serlin, C. L. Tschirhart, H. Polshyn, Y. Zhang, J. Zhu, K. Watanabe, T. Taniguchi, L. Balents, and A. F. Young, Science **367**, 900 (2020).

[6] R. Bistritzer and A. MacDonald, Proc. Natl. Acad. Sci. USA **108**, 12233 (2011).

[7] B. Roy and V. Juricic, Phys. Rev. B **99**, 121407(R) (2019).

[8] B. Lian, Z. Wang, and B. A. Bernevig, Phys. Rev. Lett. **122**, 257002 (2019).

[9] F. Wu, A. H. MacDonald, and I. Martin, Phys. Rev. Lett. **121**, 257001 (2018).

[10] Y. H. Zhang, D. Mao, Y. Cao, P. Jarillo-Herrero, and T. Senthil, Phys. Rev. B **99**, 075127 (2019).

[11] G. W. Burg, J. Zhu, T. Taniguchi, K. Watanabe, A. H. MacDonald, and E. Tutuc, Phys. Rev. Lett. **123**, 197702 (2019).

[12] C. Shen, Y. Chu, Q. Wu, N. Li, S. Wang, Y. Zhao, J. Tang, J. Liu, J. Tian, K. Watanabe, T. Taniguchi, R. Yang, Z. Meng, D. Shi, O. V. Yazyev, and G. Zhang, Nat. Phys. **16**, 520 (2020).

[13] Y. Cao, D. R. Legrain, O. R. Bigorda, J. M. Park, K. Watanabe, T. Taniguchi, and P. J. Herrero, Nature (London) **583**, 215 (2020).
[14] X. Liu, Z. Hao, E. Khalaf, J. Y. Lee, Y. Ronen, H. Yoo, D. H. Najafabadi, K. Watanabe, T. Taniguchi, A. Vishwanath, and P. Kim, Nature (London) **583**, 221 (2020).
[15] M. He, Y. Li, J. Cai, Y. Liu, K. Watanabe, T. Taniguchi, X. Xu, and M. Yankowitz, Nat. Phys. **17**, 26 (2021).
[16] G. Chen, L. Jiang, S. Wu, B. Lyu, H. Li, B. L. Chittari, K. Watanabe, T. Taniguchi, Z. Shi, J. Jung, Y. Zhang, and F. Wang, Nat. Phys. **15**, 237 (2019).
[17] G. Chen, A. L. Sharpe, P. Gallagher, I. T. Rosen, E. J. Fox, L. Jiang, B. Lyu, H. Li, K. Watanabe, T. Taniguchi, J. Jung, Z. Shi, D. Goldhaber-Gordon, Y. Zhang, and F. Wang, Nature (London) **572**, 215 (2019).
[18] M. Koshino, Phys. Rev. B **99**, 235406 (2019).
[19] I. Martin, Y. M. Blanter, and A. F. Morpurgo, Phys. Rev. Lett. **100**, 036804 (2008).
[20] F. Zhang, A. H. MacDonald, and E. J. Mele, Proc. Natl. Acad. Sci. USA **110**, 10546 (2013).
[21] C. Z. Chang, J. Zhang, X. Feng, J. Shen, Z. Zhang, M. Guo, K. Li, Y. Ou, P. Wei, L. L. Wang, Z.-Q. Ji, Y. Feng, S. Ji, X. Chen, J. Jia, X. Dai, Z. Fang, S.-C. Zhang, K. He, Y. Wang, L. Lu, X. C. Ma, and Q. K. Xue, Science **340**, 167 (2013).
[22] F. D. M. Haldane, Phys. Rev. Lett. **61**, 2015 (1988).
[23] J. Zhu, J. J. Su, and A. H. MacDonald, Phys. Rev. Lett. **125**, 227702 (2020).
[24] H. Polshyn, J. Zhu, M. A. Kumar, Y. Zhang, F. Yang, C. L. Tschirhart, M. Serlin, K. Watanabe, T. Taniguchi, A. H. MacDonald, and A. F. Young, Nature **588**, 66 (2020).
[25] A. H. Castro Neto, F. Guinea, N. M. R. Peres, K. S. Novoselov, and A. K. Geim, Rev. Mod. Phys. **81**, 109 (2009).
[26] M. Koshino, N. F. Q. Yuan, T. Koretsune, M. Ochi, K. Kuroki, and L. Fu, Phys. Rev. X **8**, 031087 (2018).
[27] J. Y. Lee, E. Khalaf, S. Liu, X. Liu, Z. Hao, P. Kim, and A. Vishwanath, Nat. Commun. **10**, 5333 (2019).
[28] J. Liu, Z. Ma, J. Gao, and X. Dai, Phys. Rev. X **9**, 031021 (2019).
[29] N. R. Chebrolu, B. L. Chittari, and J. Jung, Phys. Rev. B **99**, 235417 (2019).
[30] E. McCann and M. Koshino, Rep. Prog. Phys. **76**, 056503 (2013).
[31] J. Jung and A. H. MacDonald, Phys. Rev. B **89**, 035405 (2014).
[32] D. Xiao, J. Shi, and Q. Niu, Phys. Rev. Lett. **95**, 137204 (2005).
[33] T. Fukui, Y. Hatsugai, and H. Suzuki, J. Phys. Soc. Jpn **74**, 1674 (2005).
[34] Y. X. Wang, F. Li, and Y. M. Wu, Europhys. Lett. **105**, 17002 (2014).
[35] F. Wu and S. Das Sarma, Phys. Rev. B **101**, 155149 (2020).
[36] M. Xie and A. H. MacDonald, Phys. Rev. Lett. **124**, 097601 (2020).
[37] D. J. Thouless, M. Kohmoto, M. P. Nightingale, and M. den Nijs, Phys. Rev. Lett. **49**, 405 (1982).
[38] T. Thonhauser, D. Ceresoli, D. Vanderbilt, and R. Resta, Phys. Rev. Lett. **95**, 137205 (2005).
[39] D. Ceresoli, T. Thonhauser, D. Vanderbilt, and R. Resta, Phys. Rev. B **74**, 024408 (2006).
[40] J. Jung, A. M. Dasilva, A. H. MacDonald, and S. Adam, Nat. Commun. **6**, 6308 (2015).
[41] N. Bultinck, S. Chatterjee, and M. P. Zaletel, Phys. Rev. Lett. **124**, 166601 (2020).